JMEPEG (2008) 17:402–410
DOI: 10.1007/s11665-007-9145-9

1059-9495/$19.00

Analysis of Heat Affected Zone in Welded Aluminum Alloys Using Inverse and Direct Modeling

A.D. Zervaki, G.N. Haidemenopoulos, and S.G. Lambrakos

(Submitted May 29, 2007)

The concept of constructing parameter spaces for process control and the prediction of properties within the heat affected zone (HAZ) of welds using inverse modeling is examined. These parameter spaces can be, in principle, either independent or a function of weld process conditions. The construction of these parameter spaces consists of two procedures. One procedure entails calculation of a parameterized set of temperature histories using inverse heat transfer analysis of the heat deposition occurring during welding. The other procedure entails correlating these temperature histories with either a specific process control parameter or physical property of the weld that is measurable. Two quantitative case study analyses based on inverse modeling are presented. One analysis examines the calculation of temperature histories as a function of process control parameters. For this case, the specific process control parameter adopted as prototypical is the electron beam focal point. Another analysis compares some general characteristics of inverse and direct modeling with respect to the prediction of properties of the HAZ for deep penetration welding of aluminum alloys. For this case, the specific property adopted as prototypical is hardness. This study provides a foundation for an examination of the feasibility of constructing a parameter space for the prediction of weld properties using weld cross-section measurements that are independent of weld process conditions.

Keywords aluminum, modeling processes, welding

1. Introduction

An examination is presented of the feasibility of constructing parameter spaces for welding process control and the prediction of weld properties from measurements of weld solidification cross sections using procedures based on inverse analysis. The motivation for the use of procedures based on inverse analysis is that the inherent complexity of welding processes is such that a completely first-principles or direct modeling approach to analysis of welding processes may not be well posed in general for quantitative analysis. This includes both the nature of the interaction of the energy source with the workpiece, which is important for the design of process control algorithms, and the material response characteristics of the workpiece to energy deposition, which is important for the prediction of weld properties. This has shown to be the case especially for the quantitative calculation of thermal histories in the heat affected zone (HAZ). Thermal histories that have been calculated by inverse analysis can be adopted as source terms to models for prediction of microstructure, which can in turn be correlated with weld properties. Correlation of certain weld properties with microstructure, however, is difficult in that models based on the direct problem approach, just as in the case of the calculation of temperature histories, may be not well posed due to the inherent complexity and non-uniqueness of the relationships between these properties and microstructure. One of these properties, historically, is hardness, which because of its convenient measurability remains an important property, even though its relationship to microstructure is difficult to represent via models based on first-principles. Accordingly, an interesting question to be considered is as follows. Can inverse analysis be extended to establish a more convenient method for predictability of weld properties, such as hardness, that are based on temperature history? This question is motivated by a simple assumption that is based on observation. In that hardness is so conveniently measurable, similar to that of the solidification cross sections of welds, it follows that (like weld cross sections) measurements of hardness should be well posed for data-driven inverse analysis. It follows, therefore, that hardness should not be adopted as an output quantity of any given parametric representation, but rather according to the inverse-problem approach, as an input quantity. In the analysis that follows the feasibility, and relative convenience of using inverse models, in contrast to direct models, is examined. The analysis adopts deep-penetration electron beam welds of aluminum alloys as a prototype system for this examination.

A.D. Zervaki and **G.N. Haidemenopoulos,** Department of Mechanical Engineering, University of Thessaly, 38334 Volos, Greece; and **S.G. Lambrakos,** Materials Science and Technology Division, Code 6390, Naval Research Laboratory, Washington, DC 20375-5320. Contact e-mail: lambrakos@nrl.navy.mil.

2. Inverse Analysis of Welds

2.1 Description of Inverse Analysis Procedure

The method of inverse analysis applied in this study is described extensively elsewhere (Ref 1). For the analysis presented here this method adopts a parametric representation

of the pseudo-steady-state temperature field $T(x,y,z,\kappa,V)$ at positions (x,y,z) within the workpiece that is given by

$$T(x,y,z,\kappa)=\sum_{i=1}^{N}T_i(x,y,z,\kappa,V) \quad \text{and} \quad T(x_k,y_k,z_k,\kappa,V)=C_k, \tag{Eq 1}$$

where V is the welding speed such that $x = Vt$, κ is the thermal diffusivity and the basis functions $T_i(x,y,z,\kappa,V)$ are such that they have trends that are consistent with those of the temperature field. The constraints C_k provide for the inclusion of information concerning the shape of the solidification boundary. Consistent sets of basis functions are linear combinations of solutions to the heat conduction equation for different types of boundary conditions on the workpiece. Accordingly, for steady-state heat deposition within a structure of finite thickness a consistent basis set of functions for parametric representation of the temperature field is

$$\begin{aligned}T_k(\hat{x},\hat{x}_k,V_k) =& C(x_k,y_k,z_k)\exp\left(-\frac{V_k(x-x_k)}{2\kappa}\right)\\ &\times\left[\sum_{i=-\infty}^{\infty}\left(\frac{1}{R_i}\right)\exp\left(-\frac{V_kR_i}{2\kappa}\right)\right.\\ &\left.+\sum_{j=-\infty}^{\infty}\left(\frac{1}{R_j}\right)\exp\left(-\frac{V_kR_j}{2\kappa}\right)\right]\end{aligned} \tag{Eq 2}$$

where

$$R_i=\left[(x-x_k)^2+(y-y_k)^2+(z-2iD-z_k)^2\right]^{1/2} \tag{Eq 3}$$

$$R_j=\left[(x-x_k)^2+(y-y_k)^2+(z-2jD+z_k)^2\right]^{1/2} \tag{Eq 4}$$

and $x = Vt$. The quantity D is the thickness of the workpiece and $\hat{x}_k=(x_k,y_k,z_k)$, $k=1,\ldots,N$, are the locations of the elemental heat sources of strengths $C(x_k, y_k, z_k)$. The diffusivity is defined as $\kappa = k_c/\rho C_p$, where k_c, ρ , and C_p are the thermal conductivity, density, and specific heat, respectively. The temperature field spanning the spatial region of interest within the workpiece is optimized by minimization of the value of the objective function defined by

$$Z_T=\sum_{m=1}^{N}w_m(\max\{T(x,y_c,z_c)\}-T_c)^2, \tag{Eq 5}$$

where T_c is the target maximum temperature for positions y_c, z_c, transverse to the motion of the energy source relative to the workpiece, which is along the x-coordinate, and w_n is the weight coefficient for the nth term. For the analysis that follows the quantity T_c assumes the value of the solidus temperature of 6061-T6 aluminum, where y_c, z_c specify locations on the two-dimensional boundary of the transverse solidification cross section of a given weldment.

2.2 Significance of Upstream Boundary Constraints for Inverse Analysis

The shape and temperature distribution of a specified upstream boundary is determined by the rate of energy deposited on the surface of the workpiece Q_{HDP} and the strength of coupling γ of the energy source occurring volumetrically within the workpiece. It can be shown that for any given upstream boundary, e.g., solidification boundary, and specific values of the diffusivity κ, welding speed V, and workpiece thickness D, there exists a temperature field $T(\hat{x},\kappa,V,D)$, such that

$$\gamma Q_{HDP}=Q_{WCH}(T(\hat{x},\kappa,V,D)) \tag{Eq 6}$$

where $\hat{x}=(x,y,z)$ and Q_{WCH} is the energy that has been coupled into the workpiece, which is given by

$$Q_{WCH}=\int_{x_1}^{x_2}\int_{y_1}^{y_2}\int_{z_1}^{z_2}\left[\int_{T_A}^{T(x,y,z)}\rho(T)C_p(T)\mathrm{d}T\right]\mathrm{d}x\,\mathrm{d}y\,\mathrm{d}z \tag{Eq 7}$$

for energy deposition within a sample volume $V_S = (x_2-x_1)(y_2-y_1)(z_2-z_1)$ of the workpiece whose density and heat capacity as a function of temperature are $\rho(T)$ and $C_p(T)$, respectively. Referring to Eq 6, it is to be noted that although a characterization of the quantity γ is dependent upon the nature of the heat deposition process, a general characterization of Q_{WCH} can in principle be based only on the geometric structure of energy-deposition profiles within the workpiece and the associated temperature distributions. In the case of electron beam welding, which is considered in this analysis, the strength of coupling of energy into the workpiece γ is a nonlinear function of the electron beam power, welding speed, and beam focal point.

Referring to Fig 1 and 2, it can be observed that for conditions of full penetration there is reasonable correlation between the position of the beam focal point and the degree of energy coupling into the workpiece. For the purpose of the present analysis the beam focal point is adopted as a variable process parameter for examining the relationship between temperature history and process control. The functional dependence shown in Fig 1 and 2 demonstrates an important characteristic of energy deposition with respect to the application of inverse analysis. Specifically, that temperature histories within a workpiece are a well-defined function of weld cross section, welding speed, and thermal diffusivity, and are not uniquely related to the characteristics of the welding process or associated process conditions.

2.3 Calculation of Temperature Histories by Inverse Analysis

The analysis presented in this section is of the electron beam welds whose transverse cross sections are shown in Fig 1 and 2.

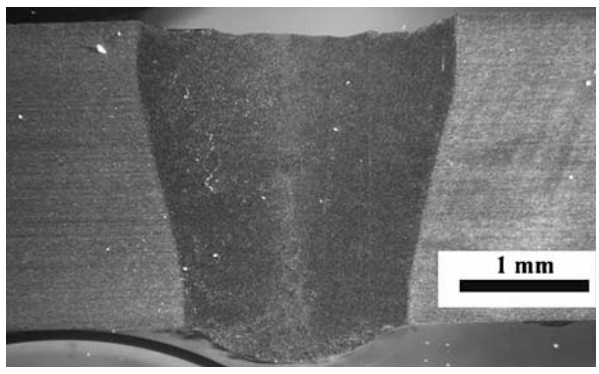

Fig. 1 Electron beam welds of Al 6061-T6 for energy deposition of 54 J/mm and beam focal point at surface of workpiece. Beam power and welding speed are 1800 W and 2000 mm/min, respectively

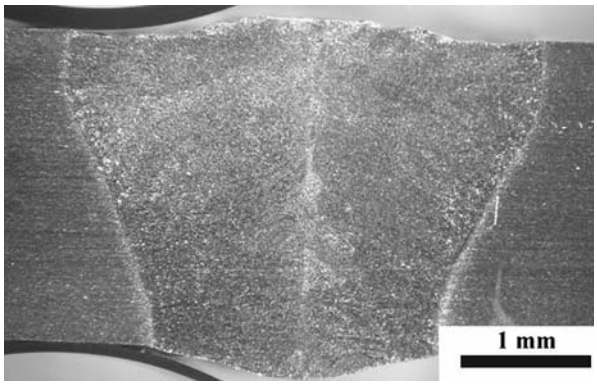

Fig. 2 Electron beam weld of Al 6061-T6 for energy deposition of 54 J/mm and beam focal point at 1 mm below top surface of workpiece. Beam power and welding speed are 1800 W and 2000 mm/min, respectively

This analysis examines the dependence of temperature history on changes in the location of the beam focal point. Before proceeding, it is significant to note that for the present analysis the exact locations of the focal points of the electron beams for the two welds are not relevant. It is important for this analysis, however, that the positions of these focal points and the associated transverse weld cross sections be noticeably different. For this analysis the model parameters are $\kappa = 1.88 \times 10^{-5}\ m^2\ s^{-1}$, $T_M = 582$ °C (solidus temperature of 6061-T6 aluminum) and $V = 3.33$ cm/s. The upstream boundary constraints on the temperature field, $T_c = T_M$ for (y_c,z_c) defined in Eq 5, are given in Table 1A and B. Shown in Fig 3 and Fig 4 are temperature histories calculated by inverse analysis for the constraint conditions given in Table 1A and B, respectively. For steady-state conditions, positions x along the direction of motion of the energy source are related to time t by $x = Vt$. The locations on the transverse cross sections of the welds, corresponding to the temperature histories shown in Fig 3 and 4, are indexed in Table 2A and B, respectively. These locations are defined relative to the lines of symmetry of the transverse solidification cross sections.

A comparison of Fig 3 and 4 indicates that, although shifted in space, the trends observed for temperature histories corresponding to both beam focal points are similar. The consideration of temperature histories as independent of weld process conditions will provide a foundation for the analysis presented in Section 5. It is significant to note that only transverse cross-section constraints were adopted for the calculation of temperature histories. Inclusion of longitudinal cross-section constraints can in principle increase sensitivity with respect to changes in value of a given process parameter, e.g., beam focal point. This follows, in principle, from the fact that the shape of the longitudinal cross section of the trailing solidification boundary is strongly correlated with the level of convective heat transfer in the weld meltpool.

3. Temperature History as a Function of Process Control Parameters

The inverse analysis presented above implies a procedure for construction of a parameter space for calculation of temperature histories as a function of process control parameters. This approach can be demonstrated by considering the functional dependence of the calculated temperature histories on electron beam focal point and spatial location within the HAZ as represented by Fig 3, 4, and Table 2. Accordingly, the functional dependence of the calculated temperature field on beam focal point at each location within the HAZ is observed to be well behaved and therefore well posed for the application of interpolation procedures associated with system parameterization. That is to say, the calculation of temperature histories by inversion of weld cross sections corresponding to a reasonably dense range of beam focal points is sufficient for prediction of temperature histories as a function of beam focal point at positions within the HAZ, and therefore construction of the function $T(x,y,x,t,$ beam focal point) is well defined. Further, it follows from Eq 6 and 7 that the strength of coupling of the energy source to the workpiece γ is also determined as a function of beam focal point. In general, full penetration of the workpiece is not expected to be achieved for a wide range of beam focal points without adjustment in values of other weld process parameters, e.g., welding speed and beam power. In that the dependence of weld characteristics on process parameters is represented implicitly, and completely, by the three-dimensional shape of the solidification boundaries of welds, construction of the multi-dimensional function $T(x,y,z,t,$ process control parameters) by inverse analysis is well defined.

Table 1 Constraint conditions (y_c, z_c) on transverse cross section of the solidification boundary for weld process conditions: 1800 W, 2000 mm/min and beam focal positions at surface of workpiece (A) and at 1 mm below top surface of workpiece (B)

A		B	
y_c (mm)	z_c (mm)	y_c (mm)	z_c (mm)
1.25	0.0	1.75	0.0
1.25	0.5	1.75	0.5
1.10	1.0	1.50	1.2
1.0	1.5	1.10	1.8
0.8	2.0	1.0	2.4
0.8	2.4		

4. Direct Modeling Using Temperature Histories

Presented in this section is a prototype simulation that demonstrates some general aspects of direct modeling of weld properties, which in this case are those microstructural features influencing hardness. The purpose of this simulation is the comparison of some general characteristics of inverse and direct modeling with respect to the prediction of properties of the HAZ. Therefore, emphasis is placed on many of the details that are necessary for direct modeling in contrast to inverse modeling.

4.1 Simulation of Microstructural Evolution in the HAZ

Welding of heat-treatable aluminum alloys, which are strengthened through precipitation hardening, is accompanied by a loss of strength in the HAZ. This degradation often places limitations on welding of these alloys. In particular, electron

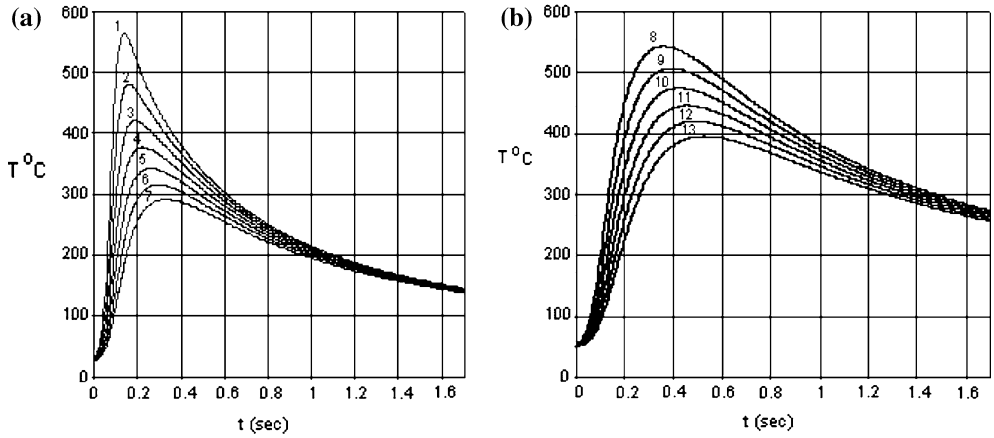

Fig. 3 Temperature histories for weld shown in Fig 1 at transverse positions indexed in Table 2A. Beam focal point at surface of workpiece

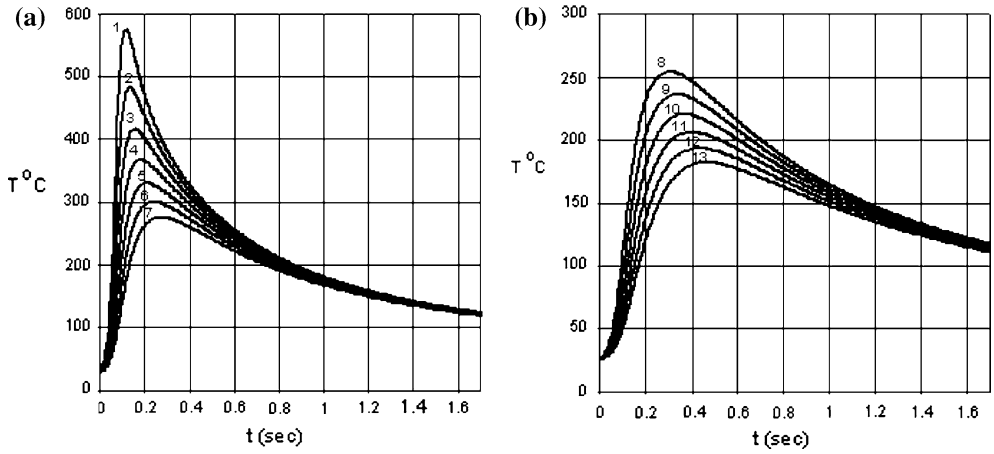

Fig. 4 Temperature histories for weld shown in Fig 2 at transverse positions indexed in Table 2B. Beam focal point at 1 mm below surface of workpiece

Table 2 Locations of calculated temperature histories on transverse cross section of weld for process conditions: 1800 W, 2000 mm/min and beam focal positions at surface of workpiece (A) and at 1 mm below top surface of workpiece (B)

	2A		2B	
Index	***y* (m)**	***z* (m)**	***y* (m)**	***z* (m)**
1	1.344×10^{-3}	3.84×10^{-4}	1.776×10^{-3}	3.84×10^{-4}
2	1.584×10^{-3}	3.84×10^{-4}	2.016×10^{-3}	3.84×10^{-4}
3	1.824×10^{-3}	3.84×10^{-4}	2.256×10^{-3}	3.84×10^{-4}
4	2.064×10^{-3}	3.84×10^{-4}	2.496×10^{-3}	3.84×10^{-4}
5	2.304×10^{-3}	3.84×10^{-4}	2.736×10^{-3}	3.84×10^{-4}
6	2.544×10^{-3}	3.84×10^{-4}	2.976×10^{-3}	3.84×10^{-4}
7	2.784×10^{-3}	3.84×10^{-4}	3.216×10^{-3}	3.84×10^{-4}
8	3.024×10^{-3}	3.84×10^{-4}	3.456×10^{-3}	3.84×10^{-4}
9	3.264×10^{-3}	3.84×10^{-4}	3.696×10^{-3}	3.84×10^{-4}
10	3.504×10^{-3}	3.84×10^{-4}	3.936×10^{-3}	3.84×10^{-4}
11	3.744×10^{-3}	3.84×10^{-4}	4.176×10^{-3}	3.84×10^{-4}
12	3.984×10^{-3}	3.84×10^{-4}	4.416×10^{-3}	3.84×10^{-4}
13	4.224×10^{-3}	3.84×10^{-4}	4.656×10^{-3}	3.84×10^{-4}

beam, or EB, welding has been applied, in heat treatable aluminum alloys. Deep penetration welding, electron and laser, has the advantage of limiting the HAZ dimensions. Despite the limited HAZ dimensions, however, a drop in HAZ hardness is still apparent. Softening in the HAZ is a common and more pronounced effect when welding with conventional welding processes. Kou (see Ref 2) observed a hardness minimum in the HAZ of gas-tungsten-arc welded 6061 alloy, welded in the artificially aged (T6) or naturally aged (T4) conditions and attributed the softening to coarsening of β'' precipitate, the

basic strengthening precipitate, and formation of the coarser β′ precipitate. Similar results have been reported (see Ref 3) on gas-metal-arc welded 6061-T6 aluminum alloy. The aim of this part of the present work is to simulate the softening reactions (dissolution and coarsening) in the HAZ of electron-beam-welded 6061-T6 aluminum alloy by an inverse analysis of weld thermal cycles in the HAZ that is combined with a computational diffusional kinetics analysis of dissolution and coarsening using the DICTRA methodology. The DICTRA (*DI*ffusion *C*ontrolled *TRA*nsformations) methodology involved (Ref 4), concerns a software for handling diffusion in multicomponent, multiphase systems based on the numerical solution of the diffusion equations assuming local thermodynamic equilibrium at the phase interfaces. Several models have been developed in the recent years to describe diffusional phase transformations in aluminum alloys. The majority of the models deal with isothermal transformations (Ref 5, 6). Relatively few research efforts have been directed towards modeling of nonisothermal transformations as those encountered in welding (Ref 7-12). The DICTRA methodology, has been applied (Ref 13) for the modeling of carbide dissolution in steels under isothermal conditions. Also DICTRA has been applied for the solution of coarsening problems under isothermal conditions (Ref 14-17). A new coarsening model, presented elsewhere (Ref 15), was implemented in DICTRA. The model was based on the assumption that coarsening of a system can be described by performing calculations on a particle of maximum size at the center of a spherical cell. The maximum particle size is 1.5 times the average size according to the LSW theory of coarsening by Lifshitz, Slyozov (Ref 18), and Wagner (Ref 19). The model was applied for the description of the coarsening behavior of carbo-nitrides in multicomponent Cr-steels under isothermal conditions (Ref 15). In the present article DICTRA is used for the simulation of dissolution, reprecipitation, and coarsening during the weld thermal cycle in the HAZ of 6061-T6 electron beam welds. The thermal cycles in the HAZ were calculated by the inverse modeling presented in the previous section. The calculated thermal cycles were used as input for the DICTRA simulations. Two assumptions were made within this work. The first assumption is that the HAZ may be characterized by two regions. One of these regions, designated HAZ_1, is where the maximum temperature of the welding cycle exceeds 400 °C and only dissolution during heating and reprecipitation during cooling can occur. The other region, designated HAZ_2, is where the maximum temperature does not exceed 400 °C and only precipitate coarsening can occur. The second assumption is that only the equilibrium precipitate β-Mg_2Si is considered in the simulations, since kinetic data for the metastable phases (GP-zones, β'', β') have not yet been included in the relevant databases.

4.2 Simulation of Dissolution During Electron Beam Welding of Al 6061-T6

The dissolution problem is treated using the DICTRA methodology. The geometrical model that was adopted is represented graphically in Fig 5. The rod morphology of the β-Mg_2Si precipitate requires the use of a cylindrical geometry. Due to reasons based on symmetry only the prescribed calculation area shown in Fig 5 was considered. In the geometrical model r_α and r_β are the radii of the α and β phase regions, respectively. The domain geometry shown in Fig 5b follows the cell model proposed by Grong (Ref 9),

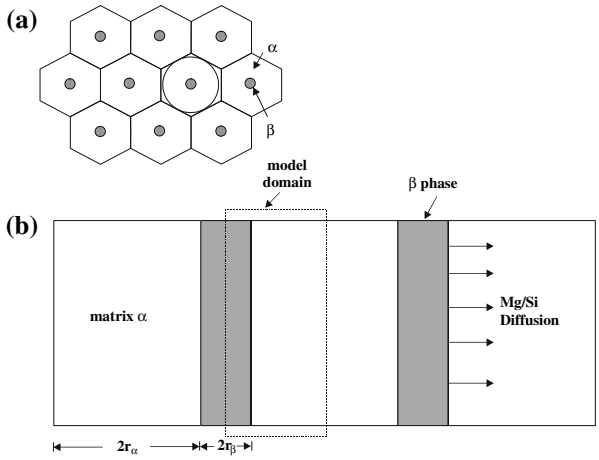

Fig. 5 Graphic representation of dissolution simulations

which is shown in Fig 5a, where each β-particle is surrounded by its own hexagonal cell and the dissolution region for the α-phase is represented by an inscribed cylinder with volume equal to that of the hexagonal cell. Further assumptions are as follows. The problem was considered to be one-dimensional where dissolution takes place only in the radial direction. Since Mg diffuses slower than Si in the α-phase (Ref 20), it was considered that only Mg diffusion controls the dissolution rate. The β-precipitate was assumed to be stoichiometric and therefore no diffusion was considered within the β-phase.

The initial compositions of the α and β phases were calculated using Thermo-Calc (see Ref 21) and obey the mass balance equations:

$$r_\alpha^0 C_{\mathrm{Mg}}^{\alpha,0} + r_\beta^0 C_{\mathrm{Mg}}^{\beta,0} = C_{\mathrm{Mg}}^0 \quad \text{(Eq 8)}$$

$$r_\alpha^0 C_{\mathrm{Si}}^{\alpha,0} + r_\beta^0 C_{\mathrm{Si}}^{\beta,0} = C_{\mathrm{Si}}^0 \quad \text{(Eq 9)}$$

where r_α^0 and r_β^0 are the initial sizes of the α and β phases, respectively, $C_{\mathrm{Mg}}^{\alpha,0}$ and $C_{\mathrm{Mg}}^{\beta,0}$ are the initial Mg contents of the α and β phases, respectively, $c_{\mathrm{Si}}^{\alpha,0}$ and $c_{\mathrm{Si}}^{\beta,0}$ are the initial Si contents of the α and β phases, respectively, and finally, c_{Mg}^0 and c_{Si}^0 are the Mg and Si alloy contents, respectively. The Mg diffusion in the α-phase ($0 < r < r_\alpha$) is described by

$$\frac{\partial c_{\mathrm{Mg}}^\alpha}{\partial t} = \frac{1}{r}\frac{\partial}{\partial r}\left(rD_{\mathrm{Mg}}^\alpha \frac{\partial C_{\mathrm{Mg}}^\alpha}{\partial r}\right) \quad \text{(Eq 10)}$$

where c_{Mg}^α and D_{Mg}^α are the Mg content and the diffusion coefficient of Mg in α-phase , respectively. The flux balance at the α/β interface is described by

$$u_{\alpha/\beta}\left(C_\beta^{\alpha/\beta} - C_\alpha^{\alpha/\beta}\right) = D_{\mathrm{Mg}}^\alpha \left(\frac{\partial C_{\mathrm{Mg}}^\alpha}{\partial r}\right)_{\alpha/\beta} \quad \text{(Eq 11)}$$

where $u_{\alpha/\beta}$ is the velocity of the α/β interface and $C_\alpha^{\alpha/\beta}, C_\beta^{\alpha/\beta}$ are the Mg concentrations of the α and β phases at the α/β interface. For this closed system the boundary conditions are

$$\left.\frac{\partial C_{\mathrm{Mg}}}{\partial r}\right|_{r=0} = 0 \quad \text{(Eq 12)}$$

and

$$\left.\frac{\partial C_{Mg}}{\partial r}\right|_{r=r_\alpha+r_\beta} = 0 \qquad \text{(Eq 13)}$$

The initial condition is given by

$$C^{\alpha}_{Mg}(r,0) = 0.88 \qquad \text{(Eq 14)}$$

for $0 \le r \le r_\alpha$ where 0.88 wt.% is the alloy Mg composition. The initial equilibrium volume fraction of the β-phase was calculated by Thermo-Calc and is $f^{o}_{\beta} = 1.45\%$. The system defined by Eq 8-14 was simulated using DICTRA for the points of the HAZ where T_{max} exceeds 400 °C. Typical results of these simulations are depicted in Fig 6 for the variation of the volume fraction during the weld thermal cycle for certain positions within HAZ_1. The corresponding thermal cycles are embedded in the same figure. The thermal cycle starts with dissolution during heating, reaches a minimum value at T_{max} and finally ends with reprecipitation during cooling. Almost complete dissolution takes place for the thermal cycle with higher T_{max}. The variation of the size r_β of the β-phase during the thermal cycle shows similar characteristics as the variation in volume fraction. Typical results are shown in Fig 7, which depicts the final mean size of the dispersion as a function of thermal cycle duration. Again here, the final size first decreases during heating and then increases during the cooling part of the thermal cycle.

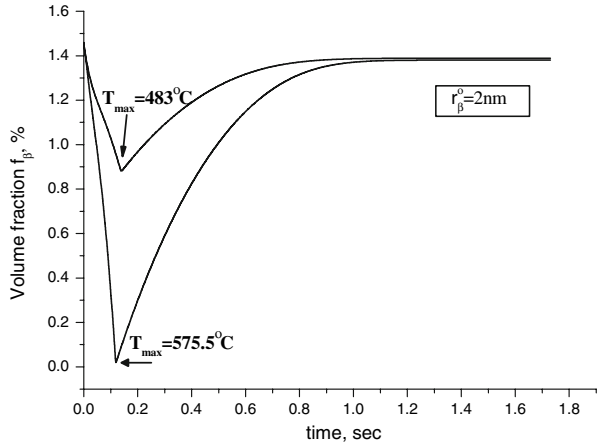

Fig. 6 Variation of volume fraction during the weld thermal cycle

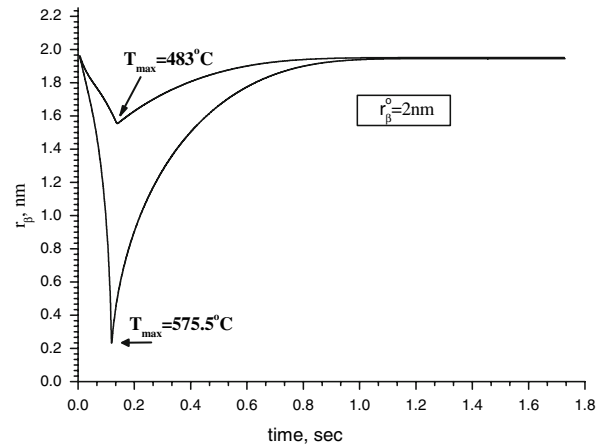

Fig. 7 Variation of mean radius of β during the weld thermal cycle

4.3 Simulation of Coarsening During Electron Beam Welding of Al 6061-T6

For these simulations the coarsening module in DICTRA was employed. According to this method coarsening of a dispersion can be described by considering one spherical particle, which has the maximum size of the dispersion prior to the application of the welding cycle. According to the LSW theory of coarsening (Ref 18,19), the maximum size r_p, is 1.5 times the mean dispersion size $\bar{r}$. The geometrical model is shown in Fig 8. The spherical particle of β-phase is embedded in a sphere of matrix α-phase. At the interface between α and β local thermodynamic equilibrium between α-phase and β-phase with radius r_p is assumed. In this case a Gibbs-Thomson contribution is added to the Gibbs free energy of the particle, which is $2\gamma V_m/r_p$, where γ is the interfacial energy of the β particle in the α-phase and V_m the molar volume. At the spherical cell boundary the α-phase is in local equilibrium with β-phase particle of the mean size $\bar{r}$, and thus the contribution to the Gibbs energy in this case is $2\gamma V_m/\bar{r}$. The difference in the Gibbs-Thomson contributions to the free energy causes diffusion of Mg and Si atoms towards the particle with radius r_p, which grows. Due to the lower diffusivity of Mg in Al, coarsening was considered to be controlled only by Mg diffusion. The interfacial energy γ was taken to be 0.5 J/m^2 (see Ref 9). In order to maintain constant volume fraction of β-phase and the initial overall alloy composition, the α-phase cell grows accordingly.

Characteristic results of the coarsening simulations are shown in Fig 9 for the case where the initial mean dispersion size is 2 nm and in Fig 10 where the initial mean dispersion size is 4 nm. The figures depict the variation of cube mean size $(\bar{r}^3)$ as a function of thermal cycle. The mean particle size increases, the change being more rapid for higher temperatures. For cycles where T_{max} is below 300 °C, particle growth is extremely slow. As expected, coarsening kinetics is faster at higher T_{max}. For a dispersion having an initial mean size of 4 nm, Fig 10 depicts similar results. Compared to the previous case of 2 nm shown in Fig 9, coarsening kinetics is slower because the initial dispersion is coarser.

4.4 Comparison of Calculated and Experimental Microhardness in HAZ

Presented in this section is a comparison between calculated and experimentally measured hardness profiles. The calculation of hardness is based on the hardness of the base metal reduced by

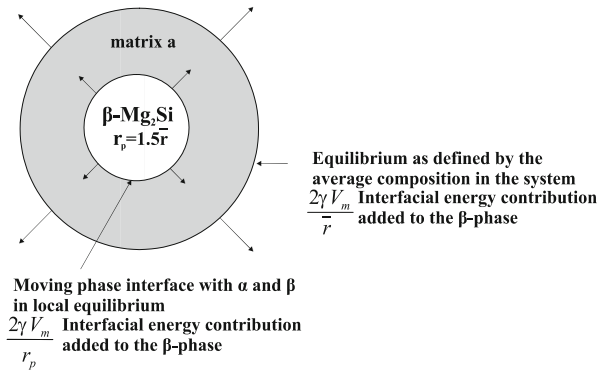

Fig. 8 Schematic representation of coarsening model incorporated into DICTRA

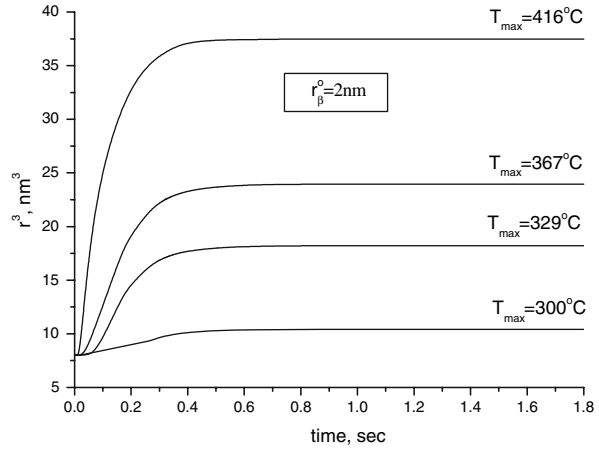

Fig. 9 Variation of $\bar{r}_\beta^3$ as a function of τ for different values of $T_{\max}(r_\beta^0 = 2\,\text{nm})$

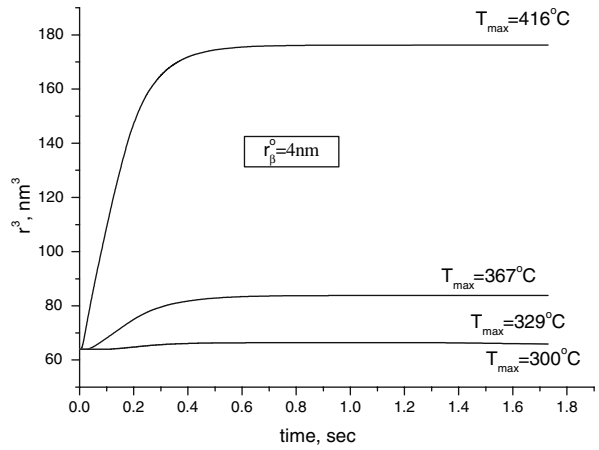

Fig. 10 Variation of $\bar{r}_\beta^3$ as a function of τ for different values of $T_{\max}(r_\beta^0 = 4\,\text{nm})$

an amount depending on the extent of dissolution or coarsening in the HAZ, which in turn depends on the final values of the volume fraction f and size r in the HAZ. Shown in Fig 11 are the calculated and experimental microhardness profiles in HAZ_1. The experimental profile was measured after EB welding with the following conditions: 1800 W, 2000 mm/min and beam focal position at surface of the workpiece. The experimental hardness profile shows that welding is accompanied by a reduction of hardness in HAZ_1. The values of $T_{\max}$, the heating rate H_R, cooling rate H_C, and thermal cycle duration τ are the input parameters of the thermal cycle for the simulation of dissolution. The simulation provides the values of f and r at the end of the thermal cycle for points within the HAZ. Precipitation hardening in HAZ_1 comes from two contributions. These are the coherency hardening, which is proportional to $f^{1/2}\,r^{1/2}$, and the Orowan hardening (obstacle bypassing), which is proportional to $f^{1/2}\,r^{-1}$. The change in hardness ΔH due to dissolution of β-phase relative to the hardness of the base metal (H_{BM}) is given by:

$$\frac{\Delta H}{H_{BM}} = \frac{f^{1/2}r^{1/2} - f_{BM}^{1/2}r_{BM}^{1/2}}{f_{BM}^{1/2}r_{BM}^{1/2}} + \frac{f^{1/2}r^{-1} - f_{BM}^{1/2}r_{BM}^{-1}}{f_{BM}^{1/2}r_{BM}^{-1}} \qquad \text{(Eq 15)}$$

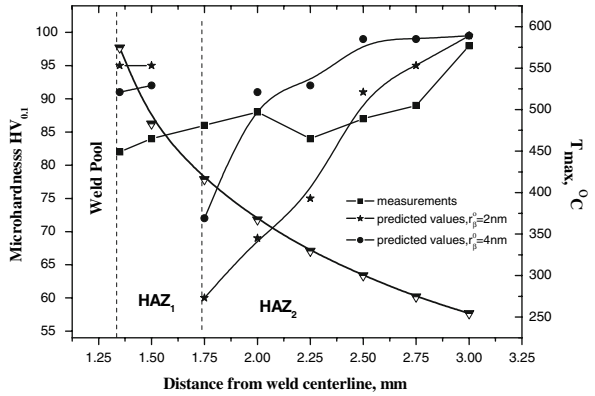

Fig. 11 Comparison of experimental and calculated microhardness values in HAZ, where the curve marked by ∇ indicates the values of $T_{\max}$

where f_{BM} = 1.45% and r_{BM} = 2 or 4 nm for the condition T6. The hardness for each point of HAZ_1 is calculated by

$$H = H_{BM} + \left(\frac{\Delta H}{H_{BM}}\right) H_{BM} \qquad \text{(Eq 16)}$$

In HAZ_2 the maximum temperature $T_{\max}$ does not exceed 400 °C and only coarsening was considered to take place. Shown in Fig 11 is the variation of the microhardness profile within HAZ_2 for calculated and experimentally measured hardness values. In order to calculate the hardness at each point within HAZ_2, it was assumed that only the Orowan mechanism is active (overaging conditions). For this case hardening is proportional to $f^{1/2}r^{-1}$. During coarsening the volume fraction f remains constant for all points of HAZ_2. Accordingly, the hardness within HAZ_2 is given by

$$H = \frac{H_{BM}r_{BM}}{r} \qquad \text{(Eq 17)}$$

The calculated hardness values are plotted with the experimental values in Fig 11. The simulation underestimates the softening of the HAZ by 16% at the interface between HAZ_1 and HAZ_2. This is attributed to the fact that only coarsening was accounted for by the observed softening in this transient region, where both phenomena are evolving. Taking into account all the assumptions made for the current simulation, the comparison with the experimental results is satisfactory. It should be noted that agreement between model prediction and experiment could be improved. The primary goal of the present analysis, however, is to examine the characteristics of a method based on direct modeling relative to those of a method based on inverse analysis.

At this stage, it is significant to restate for emphasis the primary purpose for presenting the above simulation, which has been based partially on direct modeling of microstructural features influencing hardness. This purpose was to demonstrate the inherent complexity of this modeling approach and its relative level of convenience for quantitative prediction of weld properties. Relative to this point, the feasibility of an alternative approach to the quantitative prediction of hardness is examined, which is based entirely on inverse modeling. This approach is potentially extendable to any measurable weld characteristic.

Table 3 Microhardness values $HV_{0.1}$ for process conditions: 1800 W, 2000 mm/min and beam focal position at surface of workpiece

Temperature history	T_{max} (°C)	$HV_{0.1}$
1	575.5	82
2	482.96	84
3	416.55	86
4	367.39	88
5	329.8	84
6	299.9	87
7	275.3	89
8	254.4	98
9	236.36	99
10	220.42	98
11	206.24	100
12	193.52	99
13	182.05	100

These values are presented as a function of temperature history, as indexed in Fig 3, and maximum temperature T_{max}

5. Prediction of Hardness by Inverse Analysis

Presented in this section is a general approach based on inverse analysis that implies a procedure for construction of a parameter space for quantitative prediction of hardness. This approach can be demonstrated by considering the functional dependence of the measured microhardness as represented by Table 3. Referring to this table, it can be observed that the functional dependence of the microhardness is represented as independent of position within the weld cross section. That is to say, microhardness for this alloy, for some limited range of values, has been established as a function of temperature history and maximum temperature alone. Another important aspect of this functional dependence was demonstrated by the analysis presented in Section 2.3, which demonstrated that the temperature histories are a function of weld cross section, welding speed, and thermal diffusivity, and not uniquely related to process conditions, or in general, to the welding process. Therefore, it follows that the functional dependence presented in Table 3 is independent of the welding process and of process conditions.

At this stage the feasibility of constructing a parameter space for prediction of weld properties from inverse analysis of measurements of weld cross sections is demonstrated. Accordingly, for a limited range of values, Table 3 defines microhardness as a function of temperature history and maximum temperature. In principle, this range of values can be extended arbitrarily by inverse analysis of weld cross sections corresponding to a wide range of different welding processes and process conditions. Having established the functional dependence of hardness over a sufficiently wide and dense range of temperature histories and maximum temperature values, a parameter space for the prediction of hardness for welds in general can be constructed. A extremely interesting and subtle aspect of the functionality defined by Table 3 is that it is independent of the welding process, i.e., deep penetration electron beam welding.

5.1 Hardness Measurements as Constraints on Temperature History Calculated by Inverse Modeling

The construction of Table 3 establishes a proof of concept for the existence of the process independent function $HV_{0,1}(T_{max},T(t))$. The existence of this functionality establishes a foundation for posing a significant question concerning the calculation of temperature histories by inverse modeling. To what extent can the function $HV_{0,1}(T_{max},T(t))$, having been determined for temperatures, alloy compositions and process parameters within a bounded range of values, be adopted as a global constraint for the self consistency of temperature histories calculated by inverse analysis of weld cross sections for different types of welding processes and process conditions? That is to say, a global constraint for welding processes other than those according to which the function $HV_{0,1}(T_{max},T(t))$ and its range of values have been determined.

An example of how a global constraint based on hardness could be applied in practice is as follows. We assume that a function $HV_{0,1}(T_{max},T(t))$ has been determined over a sufficiently wide range of values. We also assume that the construction of this function has evolved sufficiently through inverse analysis of a reasonably large number of different types of welds and welding processes and is therefore sufficiently accurate. Next, temperature histories are calculated by inverse analysis of weld cross sections for a given welding process, e.g., deep penetration or GMA, and values of the associated process parameters. We assume that these temperature histories have been determined by minimization of the objective function defined by Eq 5. These temperature histories imply a set of hardness values through the function $HV_{0,1}(T_{max},T(t))$ that can be compared to those hardness values that have been measured for the weld cross section subject to analysis. Accordingly, an objective function can be constructed that includes hardness measurements as constraint values. A reasonably general form for this objective function could be

$$Z = Z_T + \sum_{n=1}^{N} w_n \left(HV_{0,1}(T_{max,n}, T_n(t, y_n, z_n)) - HV_{0,1,n}(\text{measured}) \right)^2 \quad \text{(Eq 18)}$$

where Z_T is given by Eq 5, $HV_{0,1,n}(\text{measured})$ is the hardness measured at transverse location (y_n,z_n) and w_n is the weight coefficient for the nth term.

6. Conclusions

An examination of the feasibility of constructing parameter spaces for process control and the prediction of weld properties from measurements of weld cross sections has been presented. Although hardness was considered for prototype analysis, the arguments presented are applicable to any measurable weld property that is a function of temperature history. The analysis presented considered quantitative prediction of hardness of aluminum alloys using temperature histories as input to direct model simulations. An important aspect of this consideration was to examine the relative convenience of direct modeling for quantitative prediction. The results of the analysis support the feasibility of constructing parameter spaces for process control and quantitative prediction of weld properties, based entirely on

inverse analysis. This was demonstrated by the construction of Table 3, which defines a functionality that is independent of the welding process. Although the construction of the hardness function defined by Table 3 is well defined, its use as a global constraint by minimization of the objective function defined by Eq 18 is presented at this stage strictly as a hypothesis requiring further investigation. The inverse analysis approach continues to appear more conveniently applicable for quantitative analysis in practice, in contract to approaches based on direct modeling.

Acknowledgments

The authors would like to thank Mr. Vassilis Stergiou of HAI for performing EB experiments. Some of the calculations presented here (thermal histories) are based on work supported by a Naval Research Laboratory 6.1 Core program in welding. In particular, S.G.L would like to thank the Department of Mechanical Engineering at the University of Thessaly for its continued collaboration concerning welding and materials processing.

References

1. S.G. Lambrakos and J.O. Milewski, "Analysis of Welding and Heat Deposition Processes using An Inverse-Problem Approach," *Mathematical Modelling of Weld Phenomena*, **7**, p 1025, Verlag der Technischen Universite Graz, Austria, 2005
2. S. Kou, *Welding Metallurgy.* Hoboken, New Jersey, 2003, p 359–362
3. V. Malin, Aluminum Welded Joints, Study of Metallurgical Phenomena in the HAZ of 6061-T6, *Weld. J.*, 1995, **74**(9), p 305–318
4. A. Engstrom, I. Hoglud, and J. Agren, Computer Simulation of Diffusion in Multiphase Systems, *Metall. Mater. Trans.*, 1994, **25A**, p 1127–1134
5. F.J. Vermolen and C. Vuik, A Mathematical Model for the Dissolution of Particles in Multi-Component Alloys, *J. Comput. Appl. Math.*, 2000, **26**, p 233–254
6. D.H. Bratland, O. Grong, H. Schercliff, O.R. Myhr, and S. Tjotta, Modelling of Precipitation Reactions in Industrial Processing, *Acta Mater.*, 1997, **45**, p 1–22
7. M. Nicolas and A. Deschamps, Characterisation and Modelling of Precipitate Evolution in an Al-Zn-Mg Alloy During Non-Isothermal Heat Treatments, *Acta Mater.*, 2003, **51**, p 6077–6094
8. O. Grong and H. Myhr, Modelling of Non Isothermal Transformations in Alloys Containing a Particle Distribution, *Acta Mater.*, 2000, **45**, p 1–22
9. O. Grong, *Metallurgical Modelling of Welding*. The Institute of Materials, Cambridge University Press, UK, 1997, p 325–334
10. J.C. Ion, K.E. Easterling, and M.F. Ashby, A Second Report on Diagrams of Microstructure and Hardness for HAZ in Welds, *Acta Mater.*, 1984, **32**, p 1949–1962
11. B.I. Bjorneklett, O. Grong, H. Myhr, and A.O. Kluken, Additivity and Isokinetic Behavior in Relation to Particle Dissolution, *Acta Mater.*, 1998, **46**, p 6257–6266
12. M. Nicolas and A. Deschamps, Precipitate Microstructure in the Heat-Affected Zone of Al-Mn-Mg MIG-Welds and Evolution During Post Welding Heat Treatments, *Mater. Sci. Forum*, 2002, **396–402**, p 1561–1566
13. J. Agren, Kinetics of Carbide dissolution, *Scand. J. Metall.*, 1990, **9**, p 2–8
14. A. Gustafson: "Aspects of Microstructural Evolution in Chromium Steels in High Temperature Applications," Ph.D. Dissertation, KTH, Sweden, 2000
15. A. Gustafson, L. Hoglud, and J. Agren: "Simulation of Carbo-Nitride Coarsening in Multicomponent Cr-Steels for High Temperature Applications," *Advanced Heat Resistant Steels for Power Generation*. IOM Communications Ltd., London, p 270–276, 1998
16. A. Gustafson, Coarsening of TiC in Austenitic Stainless Steel-Experiments and Simulations in Comparison, *Mater. Sci. Eng.*, 2000, **A287**, p 52–58
17. A. Prikhodovski, I. Hurdado, P.J. Spencer, and D. Neuschutz: "Mathematical Simulation of Microstructure Coarsening During Preheating of Aluminium Alloys," *Proceedings of the 5th International Conference on Semi-Solid Processing of Alloys and Composites*, Colorando, p 249–256, 1998
18. I.M. Lifshitz and V.V. Slyozov, The Kinetics of Precipitation from Supersaturated Solid Solutions, *J. Phys. Chem. Solids*, 1961, **19**, p 35–50
19. C. Wagner, Theorie der Altrung von Nieederschlagen durch Umblosen (Ostwald-Reinfund), *Z. Electrochem.*, 1961, **65**, p 581–591
20. M. Bishop and K.E. Fletcher, Diffusion in Aluminium, *Int. Metall. Rev.*, 1972, **17**, p 203–225
21. B. Sudman, B. Jonsson, and J.-O. Andersson, The Thermo-Calc Databank System, *CALPHAD*, 1985, **9**, p 153